Innovative Design Research on a Cable-Driven Humanoid Robotic Arm

Zhiyuan Wu
1. State Key Laboratory of Tribology, Department of Mechanical Engineering, Tsinghua University
2. Beijing Key Lab of Precision/Ultra-precision Manufacturing Equipment and Control, Department of Mechanical Engineering, Tsinghua University
Beijing, China
zy-wu20@mails.tsinghua.edu.cn

Ye Huo
1. State Key Laboratory of Tribology, Department of Mechanical Engineering, Tsinghua University
2. Beijing Key Lab of Precision/Ultra-precision Manufacturing Equipment and Control, Department of Mechanical Engineering, Tsinghua University
Beijing, China
huoy21@mails.tsinghua.edu.cn

Kangji Ma
1. State Key Laboratory of Tribology, Department of Mechanical Engineering, Tsinghua University
2. Beijing Key Lab of Precision/Ultra-precision Manufacturing Equipment and Control, Department of Mechanical Engineering, Tsinghua University
Beijing, China
mkj21@mails.tsinghua.edu.cn

Yuanzeng Song
1. Northwestern Polytechnical University, Shaanxi, China
2. Commercial Aircraft Corporation of China Ltd, Shanghai, China
songyuanzeng@comac.cc

Haiyan Sun
1. Chengdu-Chongqin Economic Circle (Luzhou) Advanced Technology Research Institute
Luzhou, Sichuan, China
13811769703@139.com

Huaizhi Cao
1. Chengdu-Chongqin Economic Circle (Luzhou) Advanced Technology Research Institute
Luzhou, Sichuan, China
13811769703@139.com

Zhufeng Shao*
1. State Key Laboratory of Tribology, Department of Mechanical Engineering, Tsinghua University
2. Beijing Key Lab of Precision/Ultra-precision Manufacturing Equipment and Control, Department of Mechanical Engineering, Tsinghua University
Beijing, China
shaozf@mail.tsinghua.edu.cn

2024 9th International Conference on Automation, Control and Robotics Engineering (CACRE) | 979-8-3503-5030-2/24/$31.00 ©2024 IEEE | DOI: 10.1109/CACRE62362.2024.10635090

***Abstract*—The humanoid robotic arm aims to achieve multi-dimensional comprehensive similarity with the human arm in kinematics, dynamics, and physiological structure, in order to enhance human-robot collaboration capabilities and skill learning efficiency, and to realize the in-situ replacement of manual operations, holding broad application prospects. In response to the demands of human-robot interaction and unstructured environment perception, this paper, based on the analysis of the human skeletal structure and muscle driving characteristics, and considering the enveloping effect of ligaments and driving muscles on human joints, proposes a joint configuration driven by cables arranged along a spherical surface, completing the configuration design of the cable-driven humanoid robotic arm. Using spherical projection, the kinematic modeling of each joint of the cable-driven humanoid robotic arm is completed, and the kinematic performance, including workspace, is verified. The shoulder joint can achieve an inclination angle of at least 108° in any direction, with a spin angle range of at least 180°; the elbow joint has a movable range of 133°; the wrist joint can achieve an inclination angle of at least 49.5° in any direction, with a spin angle range of at least 180°, which is similar to the workspace of the human arm.**

Keywords—Humanoid Robotic Arm, Parallel Mechanism, Mechanical Design, Kinematics.

I. INTRODUCTION

With the development of modern industry, robotic arms have been widely used in multiple fields. Humanoid robotic arms, with their similarities to human arms, have shown high interactive performance with humans and are highly favored in fields that require intense human interaction, such as healthcare [1][2][3], human-robot interaction [4][5], and entertainment [6][7].

The human arm has a total of seven degrees of freedom: three at the shoulder joint, with ranges of approximately 190° to 200° for flexion and extension, as well as abduction and adduction, and approximately 90° to 120° for external and internal rotation; one at the elbow joint, with a range of about 130° to 140°; one in the forearm, with a range of about 160° to 180°; and two at the wrist joint, with a range of about 140° for flexion and extension, and about 40° to 50° for abduction and adduction. The human arm possesses characteristics such as high degrees of freedom, low inertia, large workspace, and high dynamic capabilities. Therefore, the driving and transmission scheme of humanoid robotic arms is very important. Cable-driven systems have natural advantages in terms of miniaturization, lightness, flexibility, and precision [8], and they share a high similarity with human tendons in terms of force and

motion transmission, promising to achieve driving mechanisms and kinematics similar to humans, significantly improving the overall performance of humanoid robotic arms.

In the existing joint designs of cable-driven humanoid robotic arms, the design direction can be broadly classified into two categories. One category seeks similarity with the human arm in terms of skeletal structure and driving mechanism, imitating the human skeletal structure to design the basic configuration of the robotic arm, and treating cables as human muscles, imitating the arrangement of human muscles for cable layout [9][10][11]. Due to the redundancy and complexity of human muscles, such designs often cannot perfectly replicate the arrangement of human muscles, leading to deficiencies in workspace and dynamic characteristics. These designs usually have relatively simple configuration designs and do not have the conditions for complex cable layout, and since human muscles are mostly driven by direct traction, such designs typically use a direct pull cable configuration. However, direct pull cables have a larger dynamic volume and require avoiding interference between cables and between cables and mechanisms [12], especially in the design of the shoulder joint, which is difficult to achieve a workspace similar to that of the human body due to its large working space.

The other category treats cables as a medium for transmission, designing parallel or serial rotating joints with the same degrees of freedom as the human body [13][14][15][16][17][18]. These designs do not strictly imitate the human physiological structure and, through optimization of the mechanical structure and cable layout, can significantly improve their load-bearing capacity, dynamic characteristics, and stiffness, achieving a workspace similar to that of the human body. However, these designs are usually complex and do not possess kinematic principles and driving mechanisms similar to the human body.

Therefore, how to balance a simple structural design, large workspace, and kinematics and driving mechanisms similar to the human body is one of the research issues of humanoid robotic arms.

This study will design the mechanical structure of a cable-driven humanoid robotic arm based on the structure of the human arm, conduct dynamic modeling and workspace analysis, and achieve a workspace and driving mechanism similar to that of the human arm.

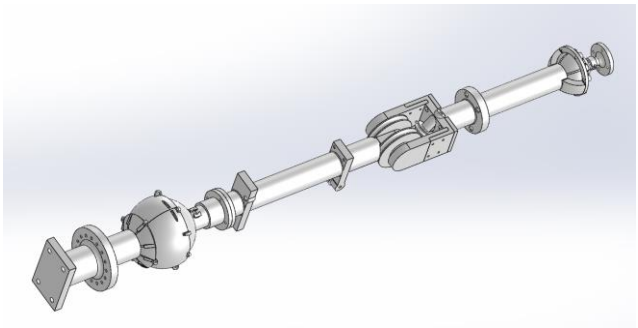

Fig. 1. The Overall Configuration of the Robotic Arm

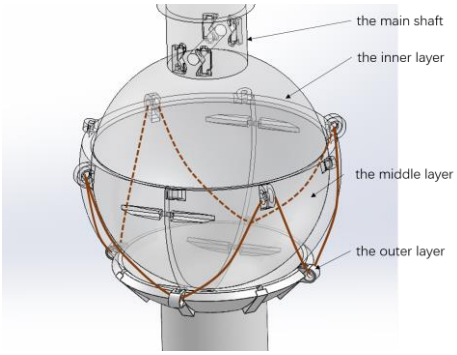

Fig. 2. The Single-Cable-Constrained Double-Layer Joint

II. Design of Cable-Driven Humanoid Robotic Arm

The overall configuration of the designed robotic arm is shown in Fig. 1.

A. Shoulder Joint Design

In order to increase the range of motion of the shoulder joint, a double-layer joint with single cable constraints is designed, mimicking the way human ligaments envelop the joint. It consists of three parts: the outer layer, the middle layer, and the inner layer (Fig. 2), which come into contact through spherical sliding. The middle and outer layers each have four equidistantly distributed cable holes through which a closed cable loop passes one by one, forming a constraint structure. Under the conditions of sufficient lubrication and tensioned cables, the linear shape of each segment of the cable can be considered as a circular arc passing through the center of the sphere, and its geometric configuration can be simplified as shown in Fig. 3. Here, α and β represent the wrap angle parameters of the middle and outer layers, respectively, with the spherical radius being r.

When the middle layer rotates around a vector $\overrightarrow{OM}$ with an angle θ to the x-axis in the x-y plane, the length of each segment of the cable changes. Taking A_1B_1 as an example, after rotation, we obtain

$$\overrightarrow{OA_1'} = \boldsymbol{T} \times \overrightarrow{OA_1} \tag{1}$$

where

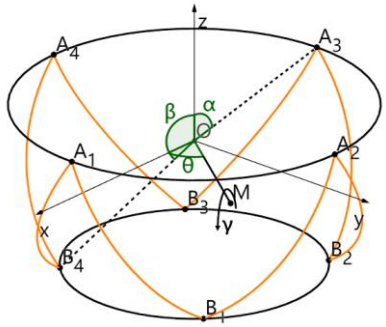

Fig. 3. The Geometric Configuration of the Single-Cable-Constrained Double-Layer Joint

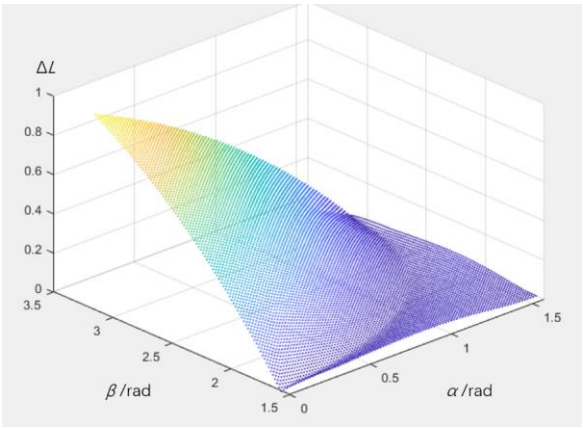

Fig. 4. The Change in Relative Length

$$\boldsymbol{T}=\begin{pmatrix}\cos\gamma+(1-\cos\gamma)\cos^2\theta & (1-\cos\gamma)\cos\theta\sin\theta & \sin\gamma\sin\theta\\ (1-\cos\gamma)\cos\theta\sin\theta & \cos\gamma+(1-\cos\gamma)\sin^2\theta & -\sin\gamma\cos\theta\\ -\sin\gamma\sin\theta & \sin\gamma\cos\theta & \cos\gamma\end{pmatrix} \tag{2}$$

and

$$\theta\in[0°,90°),\quad \gamma\in[0,\beta-\alpha) \tag{3}$$

thus

$$A_1'B_1=r\cdot\arccos\frac{\overrightarrow{OA_1'}\cdot\overrightarrow{OB_1}}{\left|\overrightarrow{OA_1'}\right|\cdot\left|\overrightarrow{OB_1}\right|} \tag{4}$$

The total length S of the cable loop can be obtained by summing up the arcs. Taking the relative length

$$L=\frac{S}{r} \tag{5}$$

The change in relative length is defined as

$$\Delta L=\frac{L_{\max}-L_{\min}}{L_{\max}} \tag{6}$$

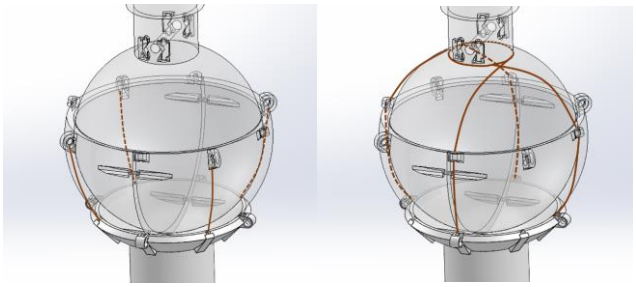

Fig. 5. The Actuation of the Shoulder Joint

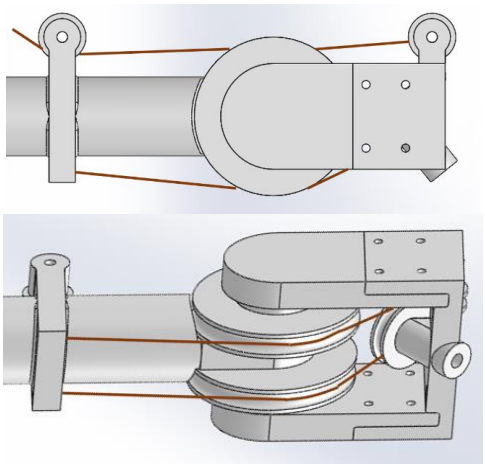

Fig. 6. The Actuation of the Elbow Joint

As shown in Fig. 4, when α is large and β is small, ΔL gets small. To expand the motion range of the joint, we take $\beta=135°$, $\alpha=77°$. Here the change is only 0.83%, which can be approximately considered as the middle layer sliding spherically with the outer layer.

To prevent interference between the direct pull cables and the mechanism during extensive joint movements, and in reference to the way muscles envelop the joints in the human body, the cables are routed along a spherical surface. This arrangement expands the range of motion of the joint, reduces the overall volume of the joint, and decreases the likelihood of interference.

For the middle layer of the shoulder joint, four cables are used to pull along the surface of the middle layer of the shoulder joint. For the inner layer of the shoulder joint, four cables are used to pull along the surface where the inner layer meets the middle layer (Fig. 5), with the cables fixed and wrapped around the main shaft, passing through holes located at the edge of the middle layer's outer surface, and reaching the outer layer. The middle layer and inner layer have two and three rotational degrees of freedom, respectively.

B. Elbow Joint Design

The muscles on the dorsal side of the elbow joint envelop the joint, while the ventral muscles are more biased towards direct traction. Referring to the layout of the muscles in the human elbow joint, the basic configuration and driving of the elbow

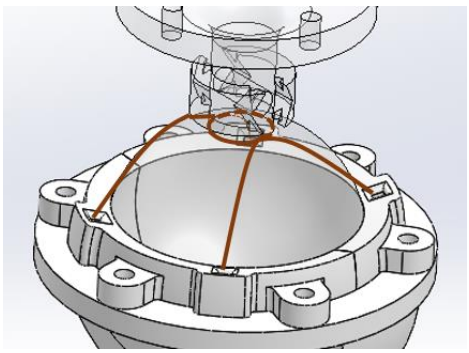

Fig. 7. The Actuation of the Elbow Joint

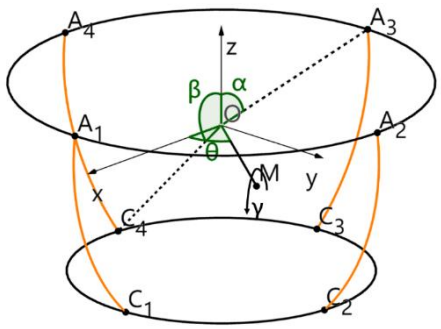

Fig. 8. The Actuation of the Elbow Joint

joint are designed (Fig. 6). This joint has one degree of rotational freedom, where the ventral cable wraps around a pulley located on the upper arm and is connected to the forearm, while the dorsal cable is guided through a fixed pulley and passes through a moving pulley.

C. Wrist Joint Design

The human forearm has one degree of freedom of spin, and the wrist joint has two degrees of freedom of rotation. In order to simplify the design and reuse the control scheme, the degree of freedom of the forearm is incorporated into the wrist joint, adopting a design approach similar to that of the inner layer of the shoulder joint. The basic configuration of the wrist joint is similar to that of the inner layer of the shoulder joint (Fig. 7), driven by four cables, which are fixed and wrapped around the main shaft, coated on the spherical surface, and pass through the points on the shell.

III. Joint Kinematic Modeling and Workspace Analysis

A. Shoulder Joint

The cable-driven layout of the middle layer of the shoulder joint can be simplified as shown in Fig. 8. Point A_1 is transformed into point A_1' after rotation. Taking A_1C_1 as an example, there is

$$A_1C_1 = r \cdot \arccos \frac{\overrightarrow{OA_1'} \cdot \overrightarrow{OC_1}}{\left|\overrightarrow{OA_1'}\right| \cdot \left|\overrightarrow{OC_1}\right|} \tag{7}$$

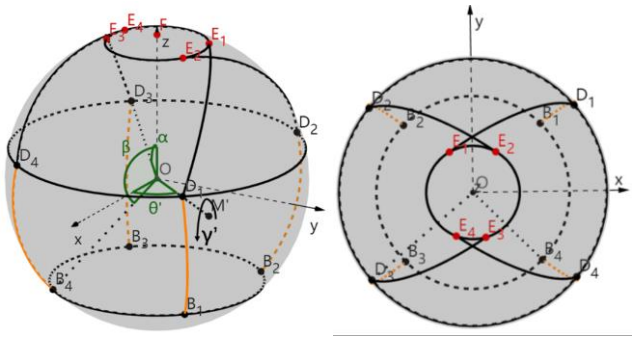

Fig. 9. The Actuation of the Shoulder Joint

By the same reasoning, the lengths of the other three cables can be obtained.

The layout and top view of the inner layer cable drive of the shoulder joint can be simplified as shown in Fig. 9, with three degrees of rotational freedom, where points E are points of tangency between the cable and the main shaft. For ease of control, a motion description method similar to the middle layer is adopted: first, rotate by an angle γ around a vector $\overrightarrow{OM'}$ that is at an angle θ to the x-axis in the $x-y$ plane, and then rotate by an angle φ around the axis of the main shaft after rotation. Taking $B_1-D_1-E_1$ as an example, it consists of two parts, one located on the surface of the middle layer and the other on the surface of the inner layer.

B_1D_1 is the part that adapts to the changes in the rotation of the middle layer, and the solution method is the same as in (7).

For the discussion of the cables on the inner layer surface, a similar concept to the polar coordinate system is used, with D_1 being the 'origin' and D_1F being the 'polar radius'. The motion of the main shaft is decomposed into distance and angle movements. The distance movement is the change in the length of , which leads to a change in the length of the tangent arc and the change in the wrapping angle of the cable around the main shaft's circle due to the movement of the tangent point. The angle movement is the rotation of the main shaft circle relative to , which leads to a change in the wrapping angle of the cable around the main shaft's circle.

Calculate the change caused by the distance movement. Taking point D_1 as the South Pole, perform a stereographic projection on the inner layer surface, projecting the main shaft circle and D_1E_1 onto a two-dimensional plane (Fig. 10). According to the nature of spherical polar projection, their projections on the plane form a line tangent to a circle. The coordinates of point F after rotation are

$$\overrightarrow{OF} = r \cdot \boldsymbol{T} \times [0,0,1]^T \tag{8}$$

The central angle opposite to D_1F is

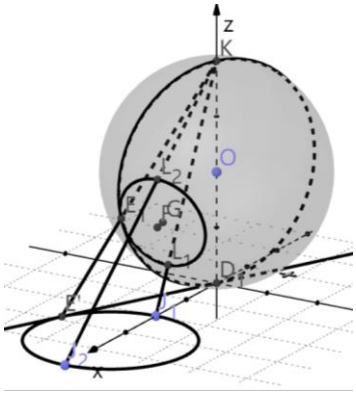

Fig. 10. The Stereographic Projection of the Inner Layer Surface

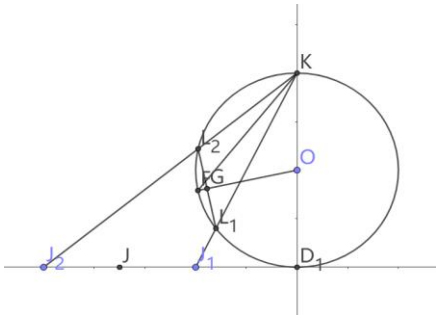

Fig. 11. The $x-z$ Section

$$\angle D_1OF = \arccos\frac{\overrightarrow{OD_1}\cdot\overrightarrow{OF}}{\left|\overrightarrow{OD_1}\right|\cdot\left|\overrightarrow{OF}\right|} \tag{9}$$

Taking the $x-z$ section as shown in Fig. 11, L_1L_2 and J_1J_2 are the diameter of the main shaft circle and its projection, respectively.

Since the central angle opposite to the same arc is twice the circumferential angle, we have

$$\angle D_1KF = \frac{1}{2}\angle D_1OF \tag{10}$$

$$\angle L_1KF = \angle L_2KF = \frac{1}{2}\angle L_1OF = \frac{1}{2}\arcsin\frac{r_z}{r} \tag{11}$$

Thus, the diameter of the projection circle is

$$J_1J_2 = 2r'[\tan(\angle L_2KF + \angle D_1KF) - \tan(\angle D_1KF - \angle L_1KF)] \tag{12}$$

The distance from the center of the projection circle to point is

$$JD_1 = r'[\tan(\angle L_2KF + \angle D_1KF) + \tan(\angle D_1KF - \angle L_1KF)] \tag{13}$$

Therefore, the length of the projection tangent $E'D_1$ is

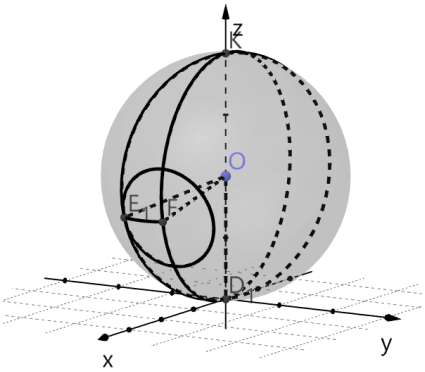

Fig. 12. The Upward Stereographic Projection

$$E'D_1 = \sqrt{JD_1^2 - \frac{1}{4}J_1J_2^2} \tag{14}$$

Thus, the central angle opposite to the arc D_1E_1 is

$$\angle D_1OE_1 = 2\angle D_1KE' = 2\arctan\frac{E'D_1}{2r} \tag{15}$$

And the length of D_1E_1 is

$$D_1E_1 = r\cdot\angle D_1OE_1 \tag{16}$$

Simultaneously with the change in the length of D_1F, the position of the tangent point E_1 and E' on the circle also changes, causing a change in the wrapping angle of the cable. For the spherical triangle $\triangle D_1E_1F$ (Fig. 12), there exists the sine theorem:

$$\frac{\sin\angle D_1E_1F}{\sin\angle D_1OF} = \frac{\sin\angle D_1FE_1}{\sin\angle D_1OE_1} = \frac{\sin\angle FD_1E_1}{\sin\angle FOE_1} \tag{17}$$

Thus, we have

$$\angle D_1FE_1 = \arcsin(\sin\angle D_1OE_1\cdot\frac{\sin\angle D_1E_1F}{\sin\angle D_1OF}) \tag{18}$$

where $\angle D_1OF$ and $\angle D_1OE_1$ are given by (9) and (15), respectively. Since D_1E_1 and the main shaft circle are tangent, $\angle D_1E_1F$ forms a right angle.

Due to the fact that in practical motion control, only the change in cable length needs to be concerned, the change in cable length caused by the distance movement can be represented as

$$L_{d1} = D_1E_1 - r\cdot\angle D_1FE_1 \tag{19}$$

For the change in cable length caused by the angle movement, take point F as the North Pole and project D_1 upwards from the South Pole point, as shown in Fig. 13.

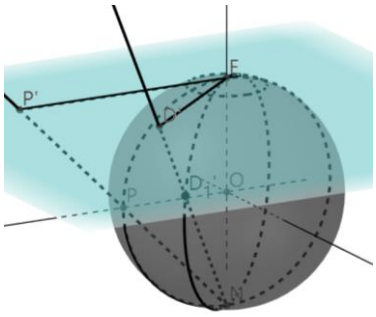

Fig. 13. The Upward Stereographic Projection

According to the properties of spherical polar projection, it is known that

$$\angle PFD_1 = \angle P'FD' \tag{20}$$

Using the inner layer as the reference frame, the coordinates of D_1 after rotation are

$$\overrightarrow{OD_1'} = \boldsymbol{T}' \times \overrightarrow{OD_1} \tag{21}$$

Let

$$\overrightarrow{OD_1'} = [x_D, y_D, z_D]^T \tag{22}$$

Then the coordinates of the projection of point D_1 on the plane are

$$\overrightarrow{FD'} = [\frac{2rx_D}{r+z_D}, \frac{2ry_D}{r+z_D}]^T \tag{23}$$

Thus

$$\angle P'FD' = \arccos \frac{\overrightarrow{FP'} \cdot \overrightarrow{FD'}}{\left|\overrightarrow{FP'}\right| \cdot \left|\overrightarrow{FD'}\right|} \tag{24}$$

Considering the angle φ of rotation of the main shaft around its own axis, the change in cable length caused by the angle movement can be represented as

$$L_{a1} = r_z \cdot (\varphi - \angle P'FD') \tag{25}$$

In summary, the length of the cable for section $B_1 - D_1 - E_1$ can be expressed as

$$L_1 = B_1D_1' + L_{d1} + L_{a1} \tag{26}$$

By the same reasoning, the lengths of the other three cables on the inner layer can be obtained.

If the motion of the joint is described as "first rotating around a vector $\overrightarrow{OM}$ in the $x-y$ plane that is inclined at an angle θ to the x-axis by an angle γ, and then rotating around the axis of the rotated main shaft by an angle φ", then for the human shoulder joint, γ can exceed 90° for almost any $\theta \in [0°, 360°)$. In this design the theoretical upper limit of φ depends only on the number of turns of the cable. For the middle layer of the shoulder joint, for any $\theta \in [0°, 360°)$, there is

$$\gamma_{\max-middle} = \beta - \alpha = 58° \tag{27}$$

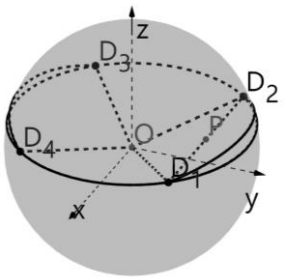

Fig. 14. The Workspace of the Shoulder Joint Inner Layer

For the inner layer of the shoulder joint, except for the two narrow regions between D_1D_2, D_3D_4 and the circle $D_1 - D_2 - D_3 - D_4$ (Fig. 14), all above the circle is reachable by the main shaft circle.

P is the midpoint of D_1D_2, and its inclination angle is

$$\gamma_P = \arctan \frac{y_P}{z_P} \tag{28}$$

By adjusting the coordinates of points D, we can obtain $\gamma_P = 70°$, so for the inner layer of the shoulder joint, $\gamma_{\max-inner} \in [70°, 77°]$

At the same time, taking the central angle of the main shaft radius as 20°, the overall maximum inclination angle of the shoulder joint

$$\gamma_{\max} = (\gamma_{\max-inner} + \gamma_{\max-middle} - 20°) \in [108°, 115°] \tag{29}$$

which can achieve a motion range similar to that of the human shoulder joint.

B. Elbow Joint

The cable-driven layout of the elbow joint can be simplified to the geometric configuration shown in Fig. 15. When the elbow joint rotates, point B rotates to point B'. Since, in practical motion control, only the change in cable length needs to be considered, considering the wrap angle of the pulley, the length of the ventral cable can be expressed as

$$L_{ventral} = B'D + r_A \cdot (\angle B'AX - \angle B'AD) \tag{30}$$

For the dorsal cable, due to the presence of the movable pulley, its cable travel needs to be doubled:

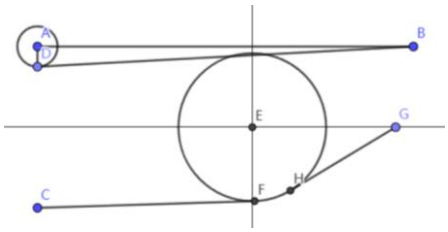

Fig. 15. The Geometric Configuration of the Elbow Joint

$$L_{dorsal} = 2r_E \cdot \alpha \tag{31}$$

Taking the coordinates of A (-80, 30) and B (60, 30), we have

$$\angle AEB = \arccos \frac{\overrightarrow{EA} \cdot \overrightarrow{EB}}{\left|\overrightarrow{EA}\right| \cdot \left|\overrightarrow{EB}\right|} = 133° \tag{32}$$

This can achieve a motion range similar to that of the human elbow joint.

C. Wrist Joint

The method for specifying the motion pattern and kinematic modeling of the wrist joint is consistent with that of the inner layer of the shoulder joint, with only the parameters changing. By adjusting the parameters, the maximum inclination angle of the wrist joint can be obtained

$$\gamma_{\max} \in [49.5°, 59.5°] \tag{33}$$

This is not entirely consistent with the motion range of the human wrist joint, but it can meet practical needs in most cases.

IV. CONCLUSION

In this paper, referring to the enveloping effect of human ligaments and muscles on joints, a cable-driven humanoid robotic arm with a workspace similar to the human body and a similar driving mechanism is designed, and kinematic modeling of its joints is carried out. The main innovations of this paper are as follows:

A single-cable-constrained double-layer spherical hinge is proposed, which has the characteristics of a large range of motion and being not easily disengaged; a four-cable three-degree-of-freedom mechanism driving along the spherical surface is proposed, which features a large workspace, compact size, and low interference.

REFERENCES

[1] Toyama, Hiroaki, Hiroaki Kawamoto, and Yoshiyuki Sankai. "Development of cybernic robot arm to realize support action cooperated with hemiplegic person's arm." *2019 41st Annual International Conference of the IEEE Engineering in Medicine and Biology Society (EMBC)*. IEEE, 2019.

[2] Zhou, Huiying, et al. "IoT-enabled dual-arm motion capture and mapping for telerobotics in home care." *IEEE journal of biomedical and health informatics* 24.6 (2019): 1541-1549.

[3] Leal-Naranjo, José Alfredo, Marco Ceccarelli, and Christopher René Torres-San Miguel. "Mechanical design of a prosthetic human arm and its dynamic simulation." *Advances in Robot Design and Intelligent Control: Proceedings of the 25th Conference on Robotics in Alpe-Adria-Danube Region (RAAD16)*. Springer International Publishing, 2017.

[4] Kousi, Niki, et al. "Enabling human robot interaction in flexible robotic assembly lines: An augmented reality based software suite." *Procedia CIRP* 81 (2019): 1429-1434.

[5] Wang, Qiyue, et al. "Virtual reality human-robot collaborative welding: A case study of weaving gas tungsten arc welding." *Journal of Manufacturing Processes* 48 (2019): 210-217.

[6] Mülling, Katharina, et al. "Learning to select and generalize striking movements in robot table tennis." *The International Journal of Robotics Research* 32.3 (2013): 263-279.

[7] Mori, Shotaro, et al. "High-speed and lightweight humanoid robot arm for a skillful badminton robot." *IEEE Robotics and Automation Letters* 3.3 (2018): 1727-1734.

[8] Wang, Yiwei, et al. "Survey on main drive methods used in humanoid robotic upper limbs." *Cyborg and Bionic Systems* (2021).

[9] Fan, Yerui, et al. "A feedforward compensation approach for cable-driven musculoskeletal systems." *Robotica* 41.4 (2023): 1221-1230.

[10] Richter, Christoph, et al. "Musculoskeletal robots: scalability in neural control." *IEEE Robotics & Automation Magazine* 23.4 (2016): 128-137.

[11] Toedtheide, Alexander, et al. "An integrated, force-sensitive, impedance controlled, tendon-driven wrist: Design, modeling, and control." *2020 IEEE-RAS 20th International Conference on Humanoid Robots (Humanoids)*. IEEE, 2021.

[12] Guckert, M. L., & Naish, M. D. (2009, October). Design of a novel 3 degree of freedom robotic joint. In *2009 IEEE/RSJ International Conference on Intelligent Robots and Systems* (pp. 5146-5152). IEEE.

[13] Kim, Y. J. (2017). Anthropomorphic low-inertia high-stiffness manipulator for high-speed safe interaction. *IEEE Transactions on robotics, 33*(6), 1358-1374.

[14] Wang, B., Zhang, T., Guan, Y., Song, Y., Liang, Z., Chen, J., & Xu, W. (2021, August). Modular design of a 7-DOF cable-driven humanoid arm. In *International Conference on Mechanical Design* (pp. 1793-1806). Singapore: Springer Nature Singapore.

[15] Huang, Y., Chen, Y., Zhang, X., Zhang, H., Song, C., & Ota, J. (2020). A novel cable-driven 7-DOF anthropomorphic manipulator. *IEEE/ASME Transactions on Mechatronics, 26*(4), 2174-2185.

[16] Suzuki, Temma, et al. "SAQIEL: Ultra-Light and Safe Manipulator with Passive 3D Wire Alignment Mechanism." *IEEE Robotics and Automation Letters* (2024).

[17] Li, Wenyang, et al. "Development of a humanoid shoulder based on 3-motor 3 degrees-of-freedom coupled tendon-driven joint module." *IEEE Robotics and Automation Letters* 6.2 (2021): 1105-1111.

[18] Pang, Shunxiang, et al. "Stiffness Optimization of Cable-Driven Humanoid Manipulators." *IEEE/ASME Transactions on Mechatronics* (2024).